Eur. Phys. J. D **15**, 189–198 (2001)

THE EUROPEAN PHYSICAL JOURNAL D

EDP Sciences

Cold rubidium molecule formation through photoassociation: A spectroscopic study of the 0_g^- long-range state of $^{87}Rb_2$

A. Fioretti[1,2], C. Amiot[3], C.M. Dion[3], O. Dulieu[3], M. Mazzoni[4], G. Smirne[1], and C. Gabbanini[1,a]

[1] Istituto di Fisica Atomica e Molecolare del C.N.R., via Alfieri 1, 56010 Ghezzano, Pisa, Italy
[2] Unità INFM, Dipartimento di Fisica, Università di Pisa, piazza Torricelli 2, 56126 Pisa, Italy
[3] Laboratoire Aimé Cotton, Université Paris-Sud, 91405 Orsay Cedex, France
[4] Istituto di Elettronica Quantistica del C.N.R., via Panciatichi 56, 50127 Firenze, Italy

Received 18 January 2001 and Received in final form 10 April 2001

Abstract. We report the detailed analysis of translationally cold rubidium molecule formation through photoassociation. Cold molecules are formed after spontaneous decay of photoexcited molecules from a laser cooled atomic sample, and are detected by selective mass spectroscopy after two-photon ionization into Rb_2^+ ions. A spectroscopic study of the $0_g^-(5S + 5P_{3/2})$ pure long-range state of $^{87}Rb_2$ is performed by detecting the ion yield as a function of the photoassociation laser frequency; the spectral data are theoretically analyzed within the semiclassical RKR approach. Molecular ionization is resonantly enhanced through either the $2^3\Pi_g$ or the $2^3\Sigma_g^+$ intermediate molecular states. Some vibrational levels of the latter electronic state are observed and assigned here for the first time. Finally, cold molecules formation rates are calculated and compared to the experimentally measured ones, and the vibrational distribution of the formed molecules in the $a^3\Sigma_u^+$ ground triplet state is discussed.

PACS. 32.80.Pj Optical cooling of atoms; trapping – 34.50.Rk Laser-modified scattering and reactions

1 Introduction

The optical cooling, trapping, and manipulation of atomic samples in the micro-Kelvin range or below [1] is now a well-mastered technique that allows important experiments in metrology, atom optics, and collisional physics and the realization of Bose-Einstein condensation in a dilute vapor. Its extension to molecules is indeed very promising, and would open a new and exciting class of experiments in chemistry and molecular physics [2].

A substantial breakthrough in the experimental exploitation of translationally cold molecules, beyond the long-standing technique of molecular beams, has been given just a few years ago when cold molecules were produced with two very different techniques. Cold cesium molecules in the μK range were obtained as a result of a photoassociative process between laser-cooled atoms [3], while paramagnetic CaH molecules in the hundreds mK range were cryogenically cooled and trapped in a magnetic trap [4]. Very recently, a third method, based on time-varying electric fields, succeeded in slowing a beam of polar molecules [5].

Photoassociation (PA) of two colliding cold atoms into an excited molecule was first proposed by Thorsheim *et al.* [9] as a possible source of translationally cold molecules. This implies the formation of excited dimers that can then spontaneously decay to their ground state while remaining translationally cold. In the experiment of reference [3], cold Cs_2 molecules in the ground triplet state were produced in a magneto-optical trap (MOT) after spontaneous decay of photoexcited molecules. The latter were obtained by photoassociating at long range a colliding pair of cold atoms with a laser red-detuned from the principal atomic transition. The ground state molecules produced were translationally and rotationally cold but in various vibrationally excited levels. In a slightly different scheme, PA of cold potassium atoms has produced cold K_2 molecules in deeply bound levels of the ground singlet state [6]; the authors successively demonstrated that the cold molecule production can be strongly enhanced by a 2-step Franck-Condon pumping through a Rydberg molecular state [7]. Finally, ground triplet state rubidium molecules have been observed in our group also as the result of PA of cold atoms in a MOT, but with a significant contribution of a three-body recombination process as well [8].

The efficiency of cold molecule formation through PA is determined by the product of the excitation probability times the decay probability to ground-state molecules, both depending on Franck-Condon factors. Recent experiments [3,8] have demonstrated that cold-molecule formation is particularly efficient when photoassociation proceeds through pure long-range excited states [10], although the process is general and different Franck-Condon pumping schemes are possible [7]. Pure long-range

[a] e-mail: carlo@ifam.pi.cnr.it

states, in which the entire vibration is situated at rather large internuclear distance, are suitable because, extending to very long range, they can be easily populated from two free atoms in a cold binary collision. In cesium, the 0_g^- and 1_u states correlated to the $6S + 6P_{3/2}$ molecular asymptote both efficiently produce cold molecules [11, 12], as their bound levels show appreciable overlap with ground-state wave functions, allowing for efficient bound-bound decay. In rubidium, only for the $0_g^-(5S + 5P_{3/2})$ state (hereafter referred to as $0_g^-(P_{3/2})$) an efficient production of cold molecules has been demonstrated and its spectroscopic study, limited to the ^{87}Rb isotope, is reported here.

The detection of ground-state cold molecules has allowed the spectroscopic investigation of the $0_g^-(P_{3/2})$ and $1_u(P_{3/2})$ states of cesium [11,12]. This technique is complementary to other PA detection techniques based either on excited state molecule ionization or on atom trap loss detection [13]. PA spectroscopy, occurring as free-to-bound transitions that couple colliding atoms to excited molecular states, provides a very high resolution, even better than bound-to-bound molecular spectra because the initial energy spread of the free cold atoms is dramatically small (a few MHz at 100 μK). Furthermore, as the repulsive barriers of high angular momentum states cannot be overcome, only a few rotational states are present in the spectrum. Due to the long de Broglie wavelength of the cold atoms, the PA process gives information not only on the excited state potentials but also on the ground-state curves. Because PA of cold atom pairs can be viewed as a vertical transition from the atomic continuum to a bound molecular state, one can consider that, for any (fixed) frequency of the photoassociating laser, PA is taking place at a particular interatomic distance.

By photoassociative spectroscopy it is possible to probe molecular states that are difficult to explore with standard bound-to-bound spectroscopy because of the low Franck-Condon factors from the ground state. In particular, pure long-range molecular states [10] such as 0_g^- and 1_u quoted above, which have both the inner and the outer classical turning points at large internuclear distances ($R > 10a_0$, where a_0 is the Bohr radius), are practically accessible only by PA spectroscopy of cold atoms. These states generally have small well depths (ranging from a fraction of, to a few tens of, cm^{-1}), that get larger for the heavier alkalis.

Two methods are commonly used in magneto-optical traps (MOTs) to record PA spectra: trap loss and ion detection. These detection approaches give quite different results because the physical processes involved are more or less dependent on the particular excited state. In the trap loss case, when the PA laser is resonant with excited molecular levels, the average number of atoms trapped in the MOT decreases because part of the vibrational energy is converted, after the spontaneous decay, into kinetic energy of the atomic pair, which may leave the trap. This produces a decrease of the atomic fluorescence emitted by the MOT, which is monitored [14,15]. This method may require a high laser intensity to induce a significant variation of the trapped atom number. Furthermore, if the deexcitation through the emission of a red-detuned photon does not heat enough the colliding atoms, they are recaptured by the MOT and no trap loss is observed. This may happen for some vibrational levels of long-range states. The second method, where the PA reaction products, or related products, are directly detected [14,16,17], requires a more complex apparatus including a laser to ionize atoms or molecules and an ion or electron detector, but it generally allows for a higher sensitivity. In particular, excited molecules can be ionized into molecular ions that are discriminated against atomic ions by time-of-flight mass spectroscopy.

Here we present a detailed analysis of the formation of cold rubidium molecules through photoassociation. In particular, a spectral study of $^{87}Rb_2$ molecules excited by PA on the red side of the $5S_{1/2} \rightarrow 5P_{3/2}$ atomic asymptote is reported. The spectra are taken using low-power diode lasers and through detection of the molecular ions, created by ionization of ground-state molecules. In Section 2, we describe our experimental apparatus. Section 3 reports the experimental spectra. In Section 4 the spectroscopic analysis of the data within the semiclassical RKR approach is performed, and a potential curve for the 0_g^- state of $^{87}Rb_2$ is derived. Section 5 reports the calculation of the PA and cold molecule production rates and the comparison with the measured ones. Finally, the resonance enhanced two-photon process which is used to ionize cold molecules allows us to estimate the distribution of the produced molecules into the vibrational levels of the lowest triplet $a^3\Sigma_u^+$ state, which we compare to the calculated one in Section 6.

2 Experimental apparatus

The experimental apparatus is sketched in Figure 1. A vapor-cell-loaded magneto-optical trap [18] is produced in a stainless-steel cell under a high-vacuum environment ($< 10^{-8}$ torr). The cell has several windows allowing for optical access and the positioning of a channeltron multiplier near the MOT. The background Rb pressure is kept typically in the 10^{-8} torr range. A trap is created at the center of a quadrupolar magnetic field, produced by two coils in an anti-Helmholtz configuration, where three pairs of counterpropagating, retroreflected laser beams (1 cm diameter), in the standard σ^+/σ^- configuration, orthogonally cross each other. The trapping laser is a 50 mW c.w. diode laser (SDL5401-G1), injection-locked by an extended cavity diode laser. This master laser, having a linewidth below 1 MHz, is frequency-locked 12 MHz to the red side of the $F = 2 \rightarrow F' = 3$ hyperfine transition of the ^{87}Rb D_2 line at 780 nm. A 5 mW DBR diode laser (Yokogawa YL78XN), tuned to the $F = 1 \rightarrow F' = 2$ D_2 line, is split into two beams and superposed to the trapping beam in two arms to avoid optical pumping into the other hyperfine level of the ground state. Some measurements have also been done on ^{85}Rb that can be trapped just by changing the locking points of the trapping and repumping lasers.

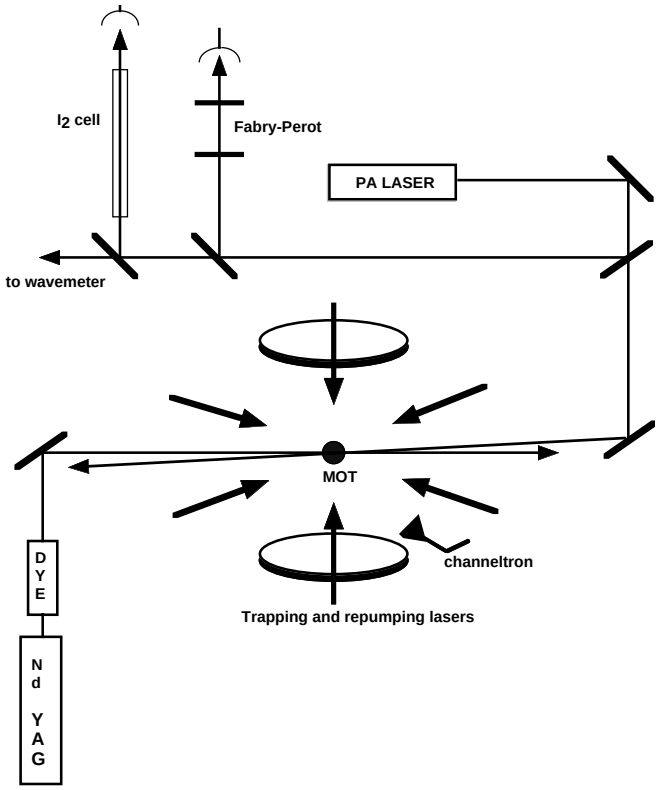

Fig. 1. Sketch of the experimental apparatus.

The MOT, being continuously monitored by a photodiode and a CCD camera, is loaded with up to $N \sim 10^7$ rubidium atoms in an almost Gaussian distribution of 0.8 mm diameter, leading to a maximum peak density $n \simeq 3 \times 10^{10}$ cm^{-3}. The atomic temperature, measured by the release and recapture method, is 120 ± 40 μK.

Several c.w. free-running diode lasers (Sanyo DL-7140-201) of 70 mW maximum output power, with a linewidth of about 30 MHz, are alternatively used as PA laser. The emission wavelength of each of them, centered near 781 nm, is continuously tuned in some range by varying the diode temperature, and is monitored by a Fabry-Perot interferometer and a λ-meter (NIST LM-10), which provide a finely calibrated relative scale and a first absolute measure of the laser wavelength, respectively. Another control on the absolute scale is obtained by sending a portion of the PA laser beam through a heated iodine cell and by detecting the absorption lines of I_2 molecules [19]. The PA laser is focused to the MOT position in a spot slightly smaller than the trap size; the resulting laser intensity is about 10 W/cm^2. A pulsed dye laser, pumped by the second harmonic of a Nd:YAG laser (7 ns pulse duration, 10 Hz repetition rate and 0.5 cm^{-1} linewidth), ionizes the cold triplet molecules through excitation to the intermediate $2^3\Pi_g(5s + 4d)$ state. The pulse energies are nearly 2 mJ with a laser beam waist of about 1 mm at the MOT position. Its wavelength is settled to the maximum of the $a^3\Sigma_u^+ \rightarrow 2^3\Pi_g$ molecular band [20], corresponding to 602.7 nm [8]. As a consequence, the ionization is sensitive to molecules in the ground triplet state but not to those in the excited states, also because of their finite lifetime.

3 Experimental spectra

By using molecular ion detection, mass selected by time-of-flight, we have recorded PA spectra for both ^{87}Rb and ^{85}Rb. We see a difference between the two isotopes in that a signal of cold $^{85}Rb_2$ molecules is detected even in absence of the PA laser. In fact, the different collisional properties of the two isotopes cause a significant molecular formation rate by three-body recombination only for ^{85}Rb [8]. For ^{87}Rb, we have recorded a quite wide PA spectrum on the red side of the $5S_{1/2} \rightarrow 5P_{3/2}$ atomic transition, as shown in Figure 2 as a function of the detuning Δ_L. To cover a significant energy range (>17 cm^{-1}) we had to use four different diode lasers; this is due to mode hops of the diode lasers that prevent a continuous tuning in some spectral regions.

One series is clearly observed and, by comparison with the trap-loss spectrum of reference [21], it is identified as the photoassociation of two free atoms to the excited molecular $0_g^-(P_{3/2})$ state. In the PA trap loss spectrum of ^{85}Rb [21], the authors, comparing the energy eigenvalues to model potentials [22], could identify three series corresponding to 0_g^-, 0_u^+ and 1_g states correlated to $5S + 5P_{3/2}$. From two of the series, accurate potentials for the $0_g^-(P_{3/2})$ and $1_g(P_{3/2})$ states were derived [23]. Here, only the $0_g^-(P_{3/2})$ state gives a significant signal of triplet ground-state molecules. The PA mechanism is similar to that observed in cesium, where the excitation of the $0_g^-(P_{3/2})$ pure long-range state is followed by a partial decay into ground-state molecules [3]. As in the case of cesium, the rubidium $0_g^-(P_{3/2})$ state has a double-well shape, with an external well ~ 28 cm^{-1} deep and a minimum at an internuclear distance $R_e \simeq 17$ Å [23], allowing for efficient PA at large internuclear distance while maintaining rather good Franck-Condon factors for decay into ground-state triplet molecules. While, for specific vibrational levels of Cs, tunneling through the internal barrier of the double well occurs [24], resulting in quite large molecule formation rates, no such effect is observed in Rb as the internal barrier is too high to be crossed through.

In PA spectroscopy, as the repulsive barriers of high angular momentum states cannot be overcome, only a few rotational states appear. In our spectrum, within a few cm^{-1} near the molecular asymptotes, the rotational structures cannot be resolved because of additional, overlapping hyperfine structure. There is also a limitation given by the diode laser linewidth, being about 30 MHz, which is larger than the natural linewidth of the $0_g^-(P_{3/2})$ state (nearly 12 MHz). However, the resolution is sufficient to partly resolve the rotational structure of the lines far detuned from the atomic resonance. In Figure 3a the rotational structure of the 0_g^- $v = 0$ vibrational level is shown, together with the rotational spectrum of the same level for ^{85}Rb. The two structures are different and reflect the presence of a g-wave shape resonance for ^{85}Rb [25] and a

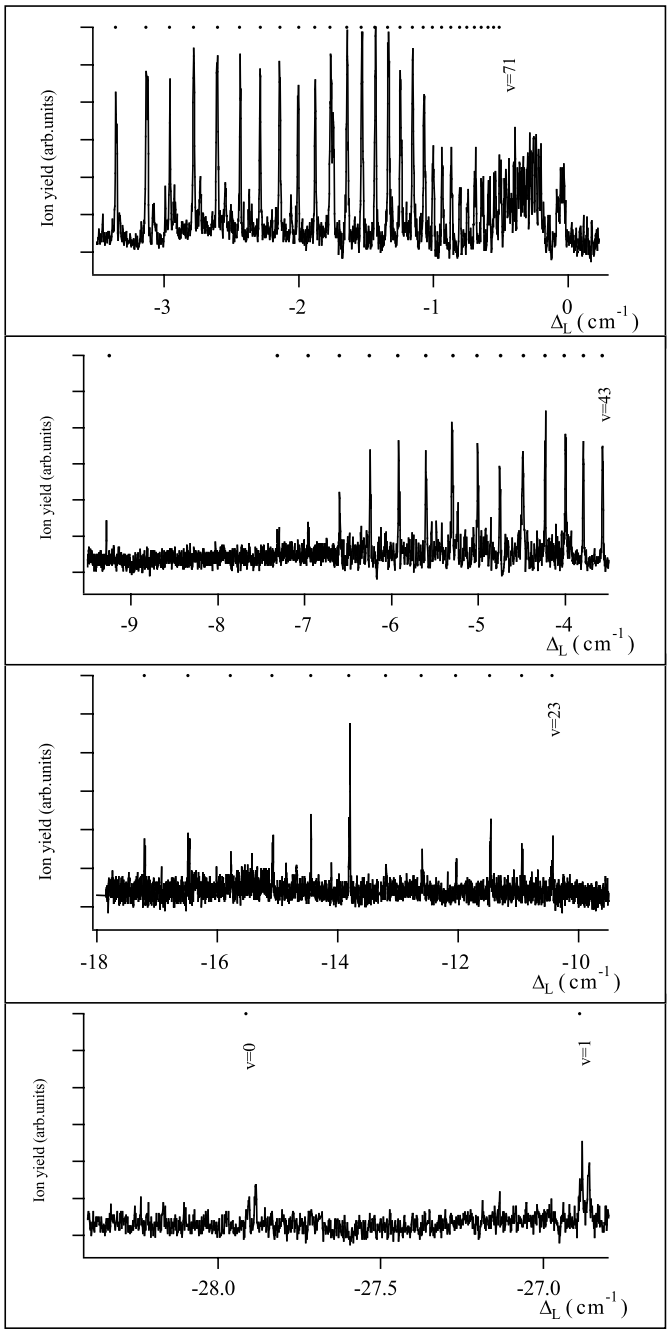

Fig. 2. PA spectrum of $^{87}Rb_2{}^+$ molecular ions on the red side of the 5S($F = 2$)–5P$_{3/2}$($F' = 3$) atomic transition, being at 12 816.47 cm^{-1}. The detuning Δ_L, with its scale changing from one graph to the other, is known with an absolute accuracy of 0.01 cm^{-1}, while the vertical scale is the same in all graphs. The $^{87}Rb_2{}^+$ yield is directly related to the $^{87}Rb_2$ cold molecule yield.

d-wave shape resonance for ^{87}Rb [26], which contribute to the $J = l, l+2, l-2$ levels. Some lower rotational levels are, in our conditions, embedded in the noise. The experimentally determined rotational constants, given in next section, are shown in Figure 3b.

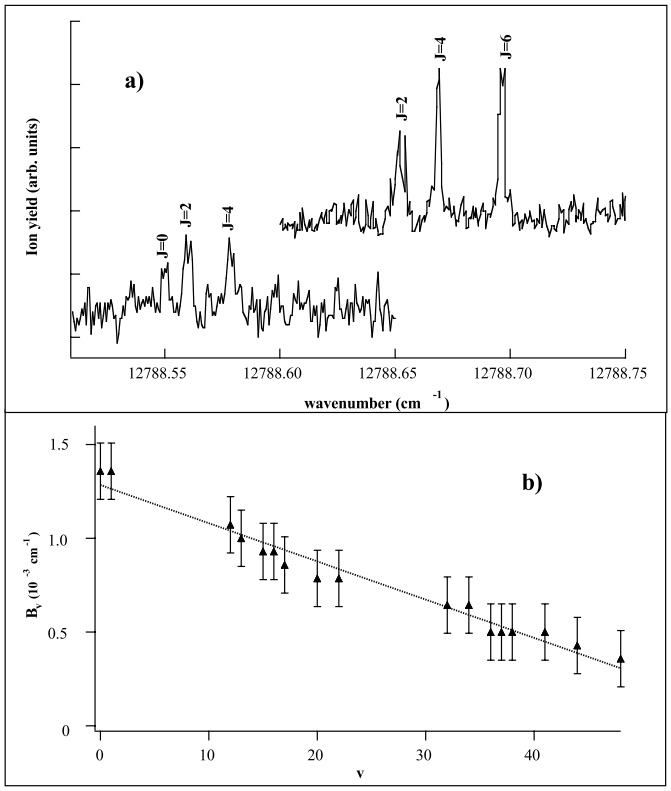

Fig. 3. (a) Rotational spectrum of the 0_g^- $v = 0$ vibrational level for ^{87}Rb (lower trace) and for ^{85}Rb (upper trace); and (b) measured rotational constant as a function of the vibrational number together with the fitted linear function reported in the text.

4 Spectroscopic analysis: RKR potential curve determination

In the previous section, vibrational levels covering most of the well depth of the $0_g^-(P_{3/2})$ potential curve (up to 0.5 cm^{-1} below the dissociation limit) were accurately measured, with a few levels missing because they lie either at the minima of the signal (*e.g.*, $v \approx 27$), or in the frequency gap between the diode lasers currently available in our group (*e.g.*, $v = 2$ to 11). From these values, we are able to determine the corresponding potential curve, which will then be used for the calculation of vibrational wave functions and molecular formation rates. The peculiar behavior of the $0_g^-(P_{3/2})$ potential curve has been described in great detail in reference [11]: for both the long-range attractive part, and the shorter range repulsive branch, it is governed mainly by a R^{-3} variation with a strength given by the asymptotic coefficient C_3. As in two previous papers [11,23], we use below two powerful tools taken from standard molecular spectroscopy: the modeling of energy levels with a Dunham polynomial expansion matched with the so-called "Near Dissociation Expansion" (NDE) analysis [27,28], which ensures a correct description of the asymptotic part of the potential curve. In Cs_2 [11], such an analysis has been found tedious for the extraction of the C_3 coefficient from measured energy

Table 1. Dunham expansion coefficients (in cm^{-1}) for the measured level energies of the $0_g^-(P_{3/2})$ long-range well of $^{87}Rb_2$. $0 \leq v \leq 71$, $0 \leq J \leq 4$.

Parameter	Value
ω_e	1.0769(11)
$10 \times \omega_e x_e$	0.1526(7)
$10^4 \times \omega_e y_e$	0.922(14)
$10^6 \times \omega_e z_e$	−0.182(10)

levels. Here, we rely on the independent determination of $C_3 = 289\,822\ (420)\ cm^{-1}Å^3$ through atomic lifetime measurements [29], which will be kept fixed during the fitting steps briefly recalled below.

4.1 The Dunham expansion of level energies

The Dunham expansion yields a complete set of energy values G_v for all vibrational levels in the observed energy range *including* the unobserved lines quoted in the previous paragraph. The experimental data consists mainly of the energies of the $v, J = 2$ levels and a few rotational levels with $J = 0$ and $J = 4$. The well-known Dunham expansion is limited here to the first order in $J(J+1)$, and to the fourth order in $(v+1/2)$, *i.e.*,

$$\begin{aligned} E(v,J) &= G_v + B_v J(J+1) \\ &= \omega_e(v+1/2) - \omega_e x_e (v+1/2)^2 \\ &\quad + \omega_e y_e (v+1/2)^3 - \omega_e z_e (v+1/2)^4 \\ &\quad + B_v J(J+1). \end{aligned} \tag{1}$$

From the few observed rotational structures (Fig. 3b) rotational constants values were obtained: $B_e^{87} = 1.28(4) \times 10^{-3}\ cm^{-1}$ and $\alpha_e^{87} = 20(9) \times 10^{-6}\ cm^{-1}$. We chose to constrain the rotational parameters for $^{87}Rb_2$ to the values derived by applying the isotopic mass relations $B_e^{87} = \rho^2 B_e^{85}$ and $\alpha_e^{87} = \rho^3 \alpha_e^{85}$ to the more accurate determinations of Heinzen [21]:

$$\begin{aligned} B_v^{85} &= B_e^{85} - \alpha_e^{85}(v+1/2) \\ &= 0.00135 - 23 \times 10^{-6}(v+1/2). \end{aligned} \tag{2}$$

After an appropriate scaling with the ratio of reduced masses $\rho = \sqrt{\mu(^{85}Rb)/\mu(^{87}Rb)} = 0.98844198$ we find $B_e^{87} = 1.32(5) \times 10^{-3}\ cm^{-1}$ and $\alpha_e^{87} = 22(2) \times 10^{-6}\ cm^{-1}$, quite close to the present experimental values $1.28 \times 10^{-3}\ cm^{-1}$ and $20 \times 10^{-6}\ cm^{-1}$. The fit of the experimental energies $E(v,J)$ includes all measured v, J levels, keeping B_e^{87} and α_e^{87} fixed to the value deduced from reference [21] with the isotopic relation. The fit reproduces the observations with a r.m.s. of the errors equal to $0.011\ cm^{-1}$, and the effective parameters are displayed in Table 1. It is worth noticing that the contribution to energy of the higher order distortion parameters $(D, H, ...)$ in equation (2) is found negligible because only transitions with low J quantum numbers are observed. The ω_e parameter is found nearly equal to the $^{85}Rb_2$ determination of reference [21]: $1.0770(1)\ cm^{-1}$. The larger uncertainty found here and the fact that the isotopic relation $\omega_e(^{87}Rb) = \rho\omega_e(^{85}Rb)$ is not fulfilled is attributed to the lack of data for vibrational levels between $v = 2$ to $v = 11$.

4.2 The NDE analysis

The determination of the $0_g^-(P_{3/2})$ potential curve requires the modeling of vibrational energies up to the dissociation limit. It is expected from previous studies [30] that the pure $C_3(0_g^-)/R^3$ long range behavior will be valid only in the region of the uppermost vibrational levels, say with a binding energy lower than $1\ cm^{-1}$. For larger binding energies, the R-variation of the $C_3(0_g^-)$ coefficient and the increase of R^{-6} and R^{-8} terms will become significant. For instance, a 1% variation of $C_3(0_g^-)$ is expected when coming from infinity towards the external turning point of the $v = 61$ level (around 65 Å), due to the interaction with the $0_g^-(P_{1/2})$ state.

It has long been known that the Dunham expansion provides only a poor extrapolation towards the dissociation limit. Le Roy and Bernstein [27] and Stwalley [28] have shown that such an analysis can be performed within the near-dissociation expansion theory (NDE), yielding accurate determination of the dissociation limit energy D_e and of the non-integer vibrational quantum number at dissociation v_D. We already recalled the main equations in [11]. Focusing on a potential with a R^{-3} long range behavior, the vibrational energy can be expanded according to the so-called outer Padé expansion, using Le Roy's notations, which is given by

$$\begin{aligned} G_v^{\rm NDE} &= D_e - X_0(3)(v_D - v)^6 [L/M] \\ &= D_e - X_0(3)(v_D - v)^6 \\ &\quad \times \frac{\left[1 + \sum_L p_L (v_D - v)^{L-1+\rm NDP1}\right]}{\left[1 + \sum_M q_M (v_D - v)^{M-1+\rm NDQ1}\right]}, \end{aligned} \tag{3}$$

where $X_0(3) = 36\,409.62/\mu^3 C_3^2$, with μ the reduced mass of the molecule, and NDP1 and NDQ1 are fixed exponents. When L (resp. M) is equal to zero the numerator (resp. the denominator) reduces to unity. Similarly, the rotational constants are expressed as:

$$B_v^{\rm NDE} = X_1(3)[v_D - v]^4 \exp\left[\sum_{l=1}^{L} p_{l1}(v_D - v)^l\right], \tag{4}$$

where $X_1(3) = 60\,221.029/\mu^3 C_3^2$. Since the data for levels lying very close to dissociation limit are lacking, it would be unreasonable to expect to determine from NDE fits meaningful values for the constant $X_0(3)$ and for the C_3 parameter. We use instead the value $C_3 = 289\,822\ (420)\ cm^{-1}\ Å^3$ quoted above, which will also contribute to lower the correlation between the other parameters (v_D, D_e, and L and M exponents) of the fit. In order to extract the NDE parameters, we introduce in equation (3) the G_v term values, calculated from the results of Table 1, referred to the bottom of the potential curve

Table 2. Parameters in the [3/0] outer Padé $G_v^{\rm NDE}$ fit of the $0_g^-(\mathrm{P}_{3/2})$ state of $^{87}Rb_2$. All digits are significant for the purpose of recomputing the G_v values. The v interval used for the fit is $v < 2, 11 < v < 23, 30 < v < 71$.

Parameter	Value	During fit
NDP1	2	fixed
$10^{-5}C_3$ (cm^{-1} Å^3)	2.89822229	fixed
$10^{11}X_0(3)$ (cm^{-1})	0.5282575367	fixed
$v_{\rm D}$	136.0622347 ± 0.217	variable
D_e (cm^{-1})	28.36482406 ± 0.006	variable
$10^5 p_1$	4.9428332547	variable
$10^7 p_2$	−7.2877289198	variable
$10^9 p_3$	2.1909286248	variable
10^3 r.m.s. (cm^{-1})	3.3	

Table 3. Parameters in the $B_v^{\rm NDE}$ fit of the $0_g^-(\mathrm{P}_{3/2})$ state of $^{87}Rb_2$. All digits are significant for the purpose of recomputing the B_v values.

Parameter	Value	During fit
$10^{-5}C_3$ (cm^{-1} Å^3)	2.89822229	fixed
$10^{11}X_1(3)$ (cm^{-1})	0.8737309800	fixed
$v_{\rm D}$	136.0622347	fixed
$10^2 p_{11}$	−0.521381495	variable
$10^4 p_{21}$	0.369404826	variable
$10^6 p_{31}$	−0.318983650	variable

$E(v = -1/2, J = 0)$. Several nonlinear NDE least-squares fits have been done using the codes of Le Roy [31–33] and selecting various combinations of $[L/M]$ Padé polynomials. A very compact expression with $L = 3$ and $M = 0$ fits the measured energy values with an r.m.s. error of about 0.003 cm^{-1} (see Tab. 2). The B_v values were calculated up to $v = 20$ using isotopic relations, and an exponential development was built according to equation (4). The parameters of the resulting fit are quoted in Table 3.

4.3 The Rydberg-Klein-Rees (RKR) potential curve

An RKR potential energy curve, *i.e.* the set of positions of the outer and inner classical turning points for the energies $G_v^{\rm NDE}$, is reported in Table 4 for computing purposes. It is worth noticing that it is constructed with calculated (*i.e.* not measured) B_v values and, as a consequence, the inner wall cannot be well defined. Above $v = 20$ the inner wall is extrapolated (in cm^{-1} with R in Å) as

$$V(R) = -0.6151 + 0.99632486 \times 10^6 \exp\left(-0.79759767R\right). \quad (5)$$

According to the NDE analysis, it should contain about 137 vibrational levels, which is close to what is predicted from the isotopic relation $v_{\rm D}^{87} = v_{\rm D}^{85}/\rho = 137.03$, applied to $v_{\rm D}^{85}$ =135.45 [23]. The well depth is also very close to the one obtained in the $^{85}Rb_2$ analysis (28.295 cm^{-1} [15]), as expected from the usual Born-Oppenheimer picture. Finally, at the present level of accuracy, it is impossible to predict any difference between the C_3 coefficient of both isotopes, which is expected to scale as the ratio of the reduced mass of the e-Rb$^+$ system $\rho_{\rm at}^{-6} = \left[\mu_{\rm at}(^{87}\mathrm{Rb})/\mu_{\rm at}(^{85}\mathrm{Rb})\right]^6 = 1.000000445$, due to the normalization of s and p atomic wave functions.

5 PA and cold molecule formation rates: calculation and experiment

The efficiency of the cold molecule formation process *via* the $0_g^-(\mathrm{P}_{3/2})$ state of Rb_2 can be investigated using a perturbative approach [34], which has been recently found to provide rates in good agreement with measured values for the cesium case [35,36]. Such a model then yields a reliable calibration procedure of rates for the present study. We briefly recall below the main steps of the model. The photoassociation rate *per atom* (expressed in s^{-1}), for a vibrational level $\left|v(0_g^-)\right\rangle$ of the 0_g^- state lying at a detuning $\Delta_{\rm L}$ below $5\mathrm{S} + 5\mathrm{P}_{3/2}$, is first computed according to:

$$\mathcal{R}_{\rm PA}(\Delta_{\rm L}) = \left(\frac{3\lambda_{\rm th}^2}{2\pi}\right)^{\frac{3}{2}} \frac{h}{2} n_{\rm at} K^2 \mathcal{A} \left|\left\langle v(0_g^-)|\chi(k_{\rm B}T)\right\rangle\right|^2, \quad (6)$$

with $\lambda_{\rm th} = h\sqrt{1/\left(3\mu k_{\rm B}T\right)}$ the thermal de Broglie wavelength (μ is the reduced mass of the system, T its temperature), $2K = 2.1 \times 10^9$ s^{-1} the atomic Rabi angular frequency for a PA laser intensity $I = 10$ W/cm^2, and $\mathcal{A}$ an angular factor including hyperfine degeneracies [34,35]. A pure s-wave initial state is assumed for simplicity, with radial wavefuntion $\chi(k_{\rm B}T)$. The cold molecule formation rate *per atom* is then obtained by considering the branching ratio to the bound levels $\left|v''(a^3\Sigma_u^+)\right\rangle$, expressed simply through Franck-Condon factors,

$$\mathcal{R}_{\rm mol}(\Delta_{\rm L}) = \mathcal{R}_{\rm PA}(\Delta_{\rm L}) \sum_{v''} \left|\left\langle v(0_g^-)|v''(a^3\Sigma_u^+)\right\rangle\right|^2, \quad (7)$$

where the sum runs over all vibrational levels v'' of the $a^3\Sigma_u^+$ state. In both equations (6) and (7), the R-dependence of the transition dipole moment is neglected, as in the cesium study [35]. Bound level energies and wave functions are calculated with the mapped Fourier grid Hamiltonian method (MFGH) [37], which is well suited for the present purpose of describing vibrational motion with very long elongation. For both rubidium isotopes, the 0_g^- state is modeled with the RKR potential obtained above and in reference [23]. The $a^3\Sigma_u^+$ potential is taken from reference [38], connected at long range to a $-C_n/R^n$ expansion including $n = 6, 8, 10$ terms. We chose the most recent determination for $C_6 = 4700$ a.u. [39], and the C_8, C_{10} values from [40]. As the spectroscopy of the $a^3\Sigma_u^+$ state is unknown, we moved slightly the repulsive wall of the potential, in order to adjust its scattering length a_T to

Table 4. Position of the inner R_v^- and outer R_v^+ turning points (in Å) of the vibrational levels lying in the $0_g^-(P_{3/2})$ long-range well of $^{87}Rb_2$, with energies G_v provided by the RKR analysis. Vibrational energies (in cm^{-1}) are referred to $E(v=-1/2, J=0)$.

v	$G_v(cm^{-1})$	R_v^-(Å)	R_v^+(Å)	v	$G_v(cm^{-1})$	R_v^-(Å)	R_v^+(Å)
0	0.534	16.371856	18.079317	36	23.142	13.345008	37.775468
1	1.580	15.867983	18.861446	37	23.431	13.329828	38.532661
2	2.597	15.552050	19.463350	38	23.708	13.315489	39.311636
3	3.585	15.312492	19.996757	39	23.972	13.301943	40.113384
4	4.544	15.117243	20.493907	40	24.224	13.289148	40.938949
5	5.475	14.951771	20.969516	41	24.465	13.277063	41.789424
6	6.379	14.808050	21.431800	42	24.694	13.265650	42.665957
7	7.256	14.681105	21.885934	43	24.913	13.254873	43.569754
8	8.106	14.567606	22.335460	44	25.121	13.244699	44.502087
9	8.931	14.465197	22.782953	45	25.319	13.235095	45.464293
10	9.730	14.372138	23.230384	46	25.507	13.226034	46.457781
11	10.504	14.287104	23.679319	47	25.686	13.217487	47.484039
12	11.254	14.209058	24.131051	48	25.855	13.209427	48.544638
13	11.980	14.137167	24.586675	49	26.016	13.201829	49.641235
14	12.682	14.070754	25.047147	50	26.169	13.194671	50.775585
15	13.362	14.009258	25.513321	51	26.313	13.187929	51.949543
16	14.019	13.952207	25.985972	52	26.450	13.181583	53.165075
17	14.654	13.899199	26.465820	53	26.579	13.175612	54.424265
18	15.267	13.849890	26.953546	54	26.701	13.169998	55.729322
19	15.859	13.803980	27.449797	55	26.816	13.164721	57.082592
20	16.431	13.761208	27.955203	56	26.925	13.159765	58.486569
21	16.983	13.721283	28.470318	57	27.027	13.155113	59.943902
22	17.514	13.683951	28.995704	58	27.123	13.150750	61.457413
23	18.027	13.648993	29.531929	59	27.214	13.146660	63.030106
24	18.521	13.616213	30.079569	60	27.299	13.142829	64.665184
25	18.996	13.585441	30.639218	61	27.379	13.139244	66.366066
26	19.454	13.556523	31.211478	62	27.454	13.135891	68.136402
27	19.894	13.529323	31.796973	63	27.524	13.132758	69.980095
28	20.317	3.503719	32.396342	64	27.590	13.129834	71.901320
29	20.724	13.479601	33.010247	65	27.652	13.127106	73.904548
30	21.114	13.456868	33.639373	66	27.709	13.124564	75.994574
31	21.489	13.435430	34.284427	67	27.762	13.122197	78.176542
32	21.848	13.415204	34.946146	68	27.812	13.119996	80.455979
33	22.193	13.396116	35.625295	69	27.859	13.117951	82.838828
34	22.523	13.378095	36.322672	70	27.902	13.116053	85.331487
35	22.839	13.361079	37.039107	71	27.942	13.114294	87.940851

the reported experimental values $a_T(^{85}Rb) = -369 \pm 16 a_0$ and $a_T(^{87}Rb) = 106 \pm 4 a_0$ [39].

Computed rates $\mathcal{R}_{PA}/\mathcal{A}$ and $\mathcal{R}_{mol}/\mathcal{A}$ are displayed in Figure 4 as a function of the red-detuning Δ_L, assuming that only the *s*-wave is contributing in the initial state. Present experimental conditions are introduced in equations (6) and (7), *i.e.*, $I = 10\ W/cm^2$, $n_{at} = 3\times10^{10}\ cm^{-3}$, and $T = 120\ \mu K$. As expected, the structure of the initial radial wave function for the atom pair is reflected by the minima in the PA rate (Fig. 4). Due to scattering length difference between the two isotopes, a node for one isotope corresponds to a maximum for the other. As already discussed in reference [35], the cold molecule formation rate as a function of Δ_L (Fig. 4c) has a roughly constant maximum value modulated by the nodal structure of the initial wave function, because the PA rate decreases as

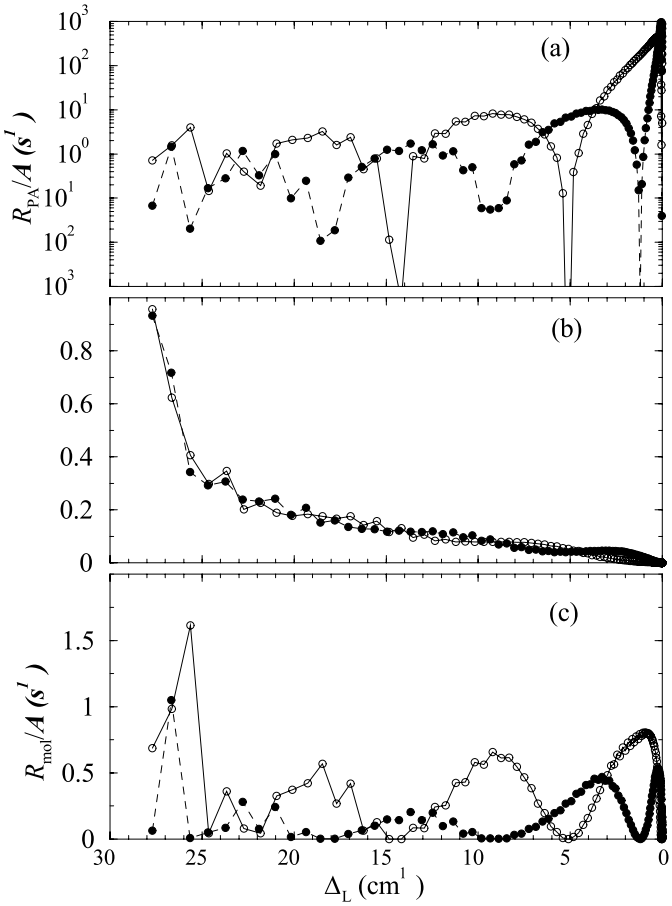

Fig. 4. Computed (a) photoassociation rate $\mathcal{R}_{\rm PA}/\mathcal{A}$, (b) branching ratio, and (c) cold molecule formation rate *per atom* $\mathcal{R}_{\rm mol}/\mathcal{A}$, as a function of the detuning $\Delta_{\rm L}$, for $^{85}Rb_2$ (open circles) and $^{87}Rb_2$ (filled circles). Present experimental conditions are used: $I = 10$ W/cm^2, $n_{\rm at} = 3 \times 10^{10}$ cm^{-3}, and $T = 120$ μK.

the red-detuning gets larger (Fig. 4a) while the branching ratio increases (Fig. 4b).

Comparing the intensity modulation of the cold molecule formation rate $\mathcal{R}_{\rm mol}(\Delta_{\rm L})$ with that observed in the ion signal (Fig. 2), we see overall a good agreement. The large minimum around 9 cm^{-1} is well reproduced, as the $0_g^-(P_{3/2})$ vibrational levels $v = 24$ to 27 are indeed not efficiently populated by PA. In contrast, the expected minimum around 1.2 cm^{-1} in Figure 4c is not visible in the experimental spectrum. To understand this discrepancy, we have performed PA rate calculations starting from other angular partial waves. With a pure p-wave initial state, the first minimum is shifted to $\Delta_{\rm L} \approx 0.8$ cm^{-1}, while none is observed in that region for a d-wave. We conclude that, in the experimental spectrum, the first minimum in the PA rate is washed out by the contribution of other partial waves.

The magnitude of the cold molecule formation rate per atom $\mathcal{R}_{\rm mol}$ can be discussed considering the similar study on cesium already quoted above [35], where the value $\mathcal{R}_{\rm mol}^{\rm Cs} \sim 0.1$ s^{-1} has been computed for $I = 55$ W/cm^2, $n_{\rm at} = 10^{11}$ cm^{-3}, $T = 140$ μK, and $\mathcal{A} \sim 0.03$. Replacing these numbers with the present experimental conditions yields $\mathcal{R}_{\rm mol}^{\rm Cs} \sim 0.007$ s^{-1}, while the Rb rate lies in 0.003–0.015 s^{-1} range (after multiplying results of Fig. 4c by $\mathcal{A} \sim 0.03$, similar to the one for Cs). Then the cold molecule formation efficiency through the 0_g^- long-range state is similar for both Cs and Rb.

As we have not included the description of the ionization steps in our model, it is difficult to compare directly intensities in Figure 4c with the experimental ones as all formed cold molecules are not expected to ionize with the same efficiency [36]. This is particularly the case for ground-state molecules found in vibrational levels lying very close to dissociation limit (binding energy smaller than 1 cm^{-1}). Their wave function is located mainly at large distances, where the electronic dipole transition moment of the first ionization step (*i.e.*, the 5S $\rightarrow$ 4D atomic transition) is almost zero. However a rough comparison between the absolute values of the computed cold molecule formation rate and the experimental one can be done. The expected cold molecule rate is obtained by multiplying the previous computed rate by the total number of trapped atoms (about 10^7), giving $3\times10^4-1.5\times10^5$ mol/s. On the experimental side, the maximum observed $^{87}Rb_2^+$ molecular ion signal due to the PA laser is about 10 ions/pulse. By considering that the molecules remain in the ionization region for nearly 10 ms [8], and that the repetition frequency of the pulsed laser is 10 Hz, the molecular production rate is about $1\,000/\eta$ s^{-1}, where η is the combined efficiency of the ionization and the detection processes. By estimating the efficiency η as being in the range 10–50% [8], the observed signal corresponds to 2×10^3–10^4 mol/s, which is about an order of magnitude below the expected one. Apart from the precise implementation of numerical factors in the calculation, we can account this difference as being primarily due to two reasons. First the PA laser is focussed in a spot slightly smaller than the MOT waist, so just a fraction of the trapped atoms contributes to the signal; second, cold molecules formed in vibrational states close to dissociation are probably very inefficiently ionized (*hidden molecules*).

6 Vibrational distribution of ultracold ground-state molecules

The vibrational distribution of the molecules produced by PA in the ground triplet state is hardly deduced from the molecular ion spectrum obtained by scanning the pulsed dye laser through the $a^3\Sigma_u^+ \rightarrow 2^3\Pi_g$ band [8]. The spin-orbit interaction that splits the $2^3\Pi_g$ state into three components [20] contributes to the complexity of the spectrum. We have found another frequency region that is appropriate to ionize the molecules in the ground triplet state. The ionization path has been assigned as connecting the Rb_2 $a^3\Sigma_u^+$ state to the molecular ion potential through the intermediate $2^3\Sigma_g^+$ state, correlating with the 5S + 4D atomic asymptote. A spectrum is shown in Figure 5, with the PA laser photoassociating ^{87}Rb through the $v = 54$

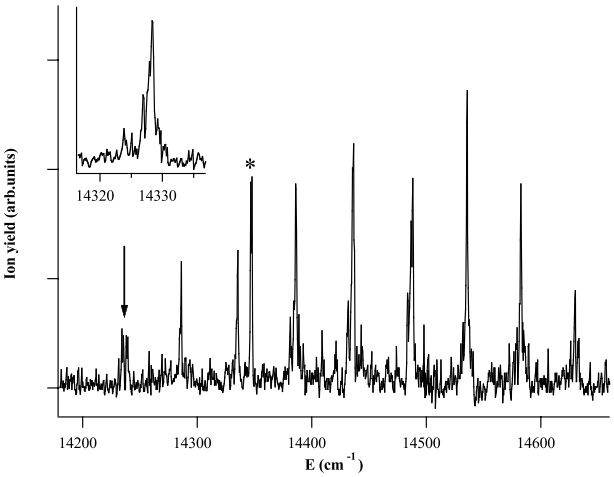

Fig. 5. Molecular ion spectrum with the PA laser tuned to the $0_g^-(P_{3/2})$ $v = 54$ vibrational level of $^{87}Rb_2$. The arrow indicates the last observed line while the peak indicated by a star is due to atomic ions when the dye laser is resonant with the 5S → 6D two-photon transition. In the blow-up one of the lines is shown in detail.

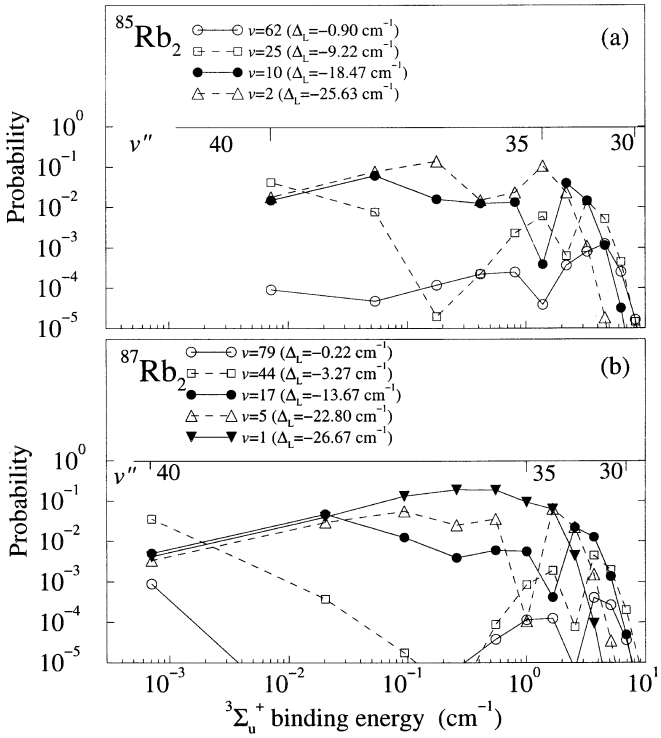

Fig. 6. Computed vibrational distributions in the lowest triplet state of (a) $^{85}Rb_2$, (b) $^{87}Rb_2$ cold molecules, for selected $0_g^-(P_{3/2})$ vibrational levels corresponding to the maxima in the cold molecule signal.

state of the $0_g^-(P_{3/2})$ state. The $2^3\Sigma_g^+$ state has never been observed up to now for Rb_2 but its potential curve has been computed in [41]. The assignment to this state has been possible because the peak separation in the spectrum is in agreement with the calculated vibrational constant ($\omega_e = 50.42$ cm^{-1}) [41], and also it must be a *gerade* state because the ions come from molecules in ground triplet state, being formed through PA and spontaneous decay from the 0_g^- state. The band structure in Figure 5 looks very simple; this is due not only to the absence of the spin-orbit interaction, but also to a narrow vibrational distribution of the cold molecular sample in the $a^3\Sigma_u^+$ state. The last observed line on the red side of the band occurs at 14 236 cm^{-1}. This line does not correspond to the excitation of the lowest vibrational level of the $2^3\Sigma_g^+$ state, but to the last vibrational level having an appreciable Franck-Condon factor with the triplet ground state potential. In fact the calculated $2^3\Sigma_g^+$ potential has a smaller equilibrium internuclear distance than the $a^3\Sigma_u^+$ state [41]. We tentatively assign the last observed line to the vibrational level $v = 11 \pm 1$.

The vibrational distribution of the formed cold molecules in the $a^3\Sigma_u^+$ state can be predicted by looking at the Franck-Condon factors in equation (7) for selected $0_g^-(P_{3/2})$ vibrational levels. Results are reported in Figure 6 for both isotopes, for the $0_g^-(P_{3/2})$ levels corresponding to the maxima of $\mathcal{R}_{mol}$. The blow-up of the experimental lines in Figure 5 confirms the hypothesis discussed above: the line has a structure which is compatible with an energy distribution of triplet vibrational levels bound by less than 5 cm^{-1}. This means that deeply bound levels are not appreciably populated. On the contrary, molecules in $a^3\Sigma_u^+$ levels bound by less than 1 cm^{-1}, that are surely populated after spontaneous emission, are probably not ionized because of the vanishing dipole moment transition, and thus are not detected.

7 Conclusion

We have presented here the first detailed analysis of the formation of cold rubidium molecules through photoassociation. The rubidium $0_g^-(5P_{3/2})$ pure long-range state, was shown to produce quite efficiently translationally cold molecules in their ground triplet state. By detecting these cold molecules by selective mass spectroscopy after two-photon ionization into Rb_2^+, a spectroscopic study of the $0_g^-(5P_{3/2})$ state has been performed for $^{87}Rb_2$. The spectral data have been theoretically analyzed within the semi-classical RKR approach and a potential curve has been derived. The cold molecule formation rates have been calculated for both rubidium isotopes showing a different dependence on the PA laser frequency due to the different scattering lengths of the two isotopes. For $^{87}Rb_2$ the structure of the computed cold molecule formation spectrum reproduces quite well the experimental one. Also the theoretical absolute magnitude of the cold molecule formation rate is in reasonable agreement with the absolute experimental rate. Finally, the ionization of the cold molecules through the intermediate $2^3\Sigma_g^+$ state, which is observed here for the first time, allows us to discuss the vibrational distribution in the ground triplet state. These observations are in agreement with the distribution predicted by

considering the Franck-Condon factors for the decay of selected 0_g^- vibrational levels into the $a^3\Sigma_u^+$ ground triplet state, which are also computed here.

Experimental activity on translationally cold molecules is getting more and more interest. In order to perform accurate experiments, efficient sources of cold molecules must be provided and suitable traps to store them must be constructed. We have shown here that in rubidium photoassociation into a pure long-range state is an efficient production possibility (like in cesium). A precise spectroscopic study of such states is thus whortwhile. A different analysis of both rubidium and cesium long-range states with purely asymptotic methods is underway in our groups.

We thank E. Arimondo, R. Pratesi, and F. Strumia for kindly lending part of the experimental equipment. Support from the Natural Sciences and Engineering Research Council (Canada) to C.M.D. and computer time from IDRIS (France) is gratefully acknowledged.

References

1. S. Chu, Rev. Mod. Phys. **70**, 685 (1998); C. Cohen-Tannoudji, *ibid.* **70**, 707 (1998); W.D. Phillips, *ibid.* **70**, 721 (1998).
2. J.T. Bahns, P.L. Gould, W.C. Stwalley, Adv. At. Mol. Opt. Phys. **42**, 171 (2000).
3. A. Fioretti, D. Comparat, A. Crubellier, O. Dulieu, F. Masnou-Seeuws, P. Pillet, Phys. Rev. Lett. **80**, 4402 (1998).
4. J.D. Weinstein, R. deCarvalho, T. Guillet, B. Friedrich, J.M. Doyle, Nature **395**, 148 (1998).
5. H.L. Bethlem, G. Berden, G. Meijer, Phys. Rev. Lett. **83**, 1558 (1999).
6. A.N. Nikolov, E.E. Eyler, X.T. Wang, J. Li, H. Wang, W.C. Stwalley, P.L. Gould, Phys. Rev. Lett. **82**, 703 (1999).
7. A.N. Nikolov, J.R. Ensher, E.E. Eyler, H. Wang, W.C. Stwalley, P.L. Gould, Phys. Rev. Lett. **84**, 246 (2000).
8. C. Gabbanini, A. Fioretti, A. Lucchesini, S. Gozzini, M. Mazzoni, Phys. Rev. Lett. **84**, 2814 (2000).
9. H.R. Thorsheim, J. Weiner, P.S. Julienne, Phys. Rev. Lett. **58**, 2420 (1987).
10. W.C. Stwalley, Y.H. Uang, G. Pichler, Phys. Rev. Lett. **41**, 1164 (1978).
11. A. Fioretti, D. Comparat, C. Drag, C. Amiot, O. Dulieu, F. Masnou-Seeuws, P. Pillet, Eur. Phys. J. D **5**, 389 (1999).
12. D. Comparat, C. Drag, B. Laburthe Tolra, A. Fioretti, P. Pillet, A. Crubellier, O. Dulieu, F. Masnou-Seeuws, Eur. Phys. J. D **11**, 59 (2000).
13. P.D. Lett, P.S. Julienne, W.D. Phillips, Annu. Rev. Phys. Chem. **46**, 423 (1995); W.C. Stwalley, H. Wang, J. Mol. Spectrosc. **195**, 194 (1999).
14. P.D. Lett, K. Helmerson, W.D. Phillips, L.P. Ratcliff, S.L. Rolston, M.E. Wagshul, Phys. Rev. Lett. **71**, 2200 (1993).
15. J.D. Miller, R.A. Cline, D.J. Heinzen, Phys. Rev. Lett. **71**, 2204 (1993).
16. D. Leonhardt, J. Weiner, Phys. Rev. A **52**, R4334 (1995).
17. H. Wang, P.L. Gould, W.C. Stwalley, Phys. Rev. Lett. **80**, 476 (1998).
18. C. Monroe, W. Swann, H. Robinson, C. Wieman, Phys. Rev. Lett. **65**, 1571 (1990).
19. S. Gerstenkorn, J. Vergès, J. Chevillard, *Atlas du spectre d'absorption de la molécule d'iode* (Laboratoire Aimé Cotton, Orsay, France, 1982).
20. G. Pichler, S. Milosevic, D. Veza, R. Beuc, J. Phys. B **16**, 4619 (1983).
21. R.A. Cline, J.D. Miller, D.J. Heinzen, Phys. Rev. Lett. **73**, 632 (1994).
22. B. Bussery, M. Aubert-Frécon, J. Mol. Spectrosc. **113**, 21 (1985).
23. C. Amiot, Chem. Phys. Lett. **241**, 133 (1995).
24. M. Vatasescu, O. Dulieu, C. Amiot, D. Comparat, C. Drag, V. Kokoouline, F. Masnou-Seeuws, P. Pillet, Phys. Rev. A **61**, 044701 (2000).
25. H.M.J.M. Boesten, C.C. Tsai, B.J. Verhaar, D.J. Heinzen, Phys. Rev. Lett. **77**, 5194 (1996).
26. H.M.J.M. Boesten, C.C. Tsai, J.R. Gardner, D.J. Heinzen, B.J. Verhaar, Phys. Rev. A **55**, 636 (1997).
27. R.J. Le Roy, R.B. Bernstein, J. Chem. Phys. **52**, 3869 (1970).
28. W.C. Stwalley, Chem. Phys. Lett. **6**, 241 (1970).
29. J.E. Simsarian, L.A. Orozco, G.D. Sprouse, W.Z. Zhao, Phys. Rev. A **57**, 2448 (1998).
30. M. Aubert-Frécon, G. Hadinger, S. Magnier, S. Rousseau, J. Mol. Spectrosc. **188**, 182 (1998).
31. R.J. Le Roy, University of Waterloo Report, Chemical Physics Research Report, Vol. CP-425, 1993.
32. R.J. Le Roy, University of Waterloo Report, Chemical Physics Research Report, Vol. CP-555, 1995.
33. Computer codes which perform the NDE fits were kindly supplied to C.A. by Pr. Le Roy.
34. P. Pillet, A. Crubellier, A. Bleton, O. Dulieu, P. Nosbaum, I. Mourachko, F. Masnou-Seeuws, J. Phys. B **30**, 2801 (1997).
35. C. Drag, B. Laburthe Tolra, O. Dulieu, D. Comparat, M. Vatasescu, S. Boussen, S. Guibal, A. Crubellier, P. Pillet, IEEE J. Quant. Electron. **36**, 1378 (2000).
36. C.M. Dion, C. Drag, O. Dulieu, B. Laburthe Tolra, F. Masnou-Seeuws, P. Pillet, Phys. Rev. Lett. **86**, 2253 (2001).
37. V. Kokoouline, O. Dulieu, R. Kosloff, F. Masnou-Seeuws, J. Chem. Phys. **110**, 9865 (1999).
38. M. Foucrault, P. Millié, J.-P. Daudey, J. Chem. Phys. **96**, 1257 (1992).
39. J.L. Roberts, N.R. Claussen, J.P. Burke, C.H. Greene, E.A. Cornell, C.E. Wieman, Phys. Rev. Lett. **81**, 5109 (1998).
40. M. Marinescu, A. Dalgarno, Phys. Rev. A **52**, 311 (1995).
41. F. Spiegelmann, D. Pavolini, J.-P. Daudey, J. Phys. B **22**, 2465 (1989).